Quantifying Chemical Composition and Reaction Kinetics of Individual Colloidally Dispersed Nanoparticles

Nathan D. Donahue[1], Sandy Kanapilly[2], Chady Stephan[3], M. Caleb Marlin[4], Emmy R. Francek[1], Majood Haddad[1], Joel Guthridge[4,5], and Stefan Wilhelm*[1,6,7]

[1] Stephenson School of Biomedical Engineering, University of Oklahoma, Norman, Oklahoma, 73019, USA

[2] PerkinElmer, Waltham, MA, 02451, USA

[3] PerkinElmer, Woodbridge, ON, L4L8H1, Canada

[4] Arthritis and Clinical Immunology, Oklahoma Medical Research Foundation, Oklahoma City, Oklahoma 73104, USA

[5] Department of Pathology, University of Oklahoma Health Sciences Center, Oklahoma City, OK, USA

[6] Institute for Biomedical Engineering, Science, and Technology (IBEST), Norman, Oklahoma, 73019, USA

[7] Stephenson Cancer Center, Oklahoma City, Oklahoma, 73104, USA

* Corresponding author: Stefan Wilhelm, Ph.D.

Email: stefan.wilhelm@ou.edu

ORCIDs of authors:

Nathan D. Donahue	0000-0003-0251-0226
Sandy Kannapilly	0000-0003-3840-1910
M. Caleb Marlin	0000-0003-0453-5355
Emmy Francek	0000-0001-8850-3582
Joel Guthridge	0000-0002-9308-237X
Stefan Wilhelm	0000-0003-2167-6221

Abstract

To control a nanoparticle's chemical composition and thus function, researchers require readily-accessible and economical characterization methods that provide quantitative *in situ* analysis of individual nanoparticles with high throughput. Here, we established dual analyte single particle inductively coupled plasma quadrupole mass spectrometry to quantify the chemical composition and reaction kinetics of individual colloidal nanoparticles. We determined the individual bimetallic nanoparticle mass and chemical composition changes during two different chemical reactions: (i) nanoparticle etching, and (ii) element deposition on nanoparticles at a rate of 300+ nanoparticles/minute. Our results revealed the heterogeneity of chemical reactions at the single nanoparticle level. This proof-of-concept study serves as a framework to quantitatively understand the dynamic changes of physicochemical properties that individual nanoparticles undergo during chemical reactions using a commonly-available mass spectrometer. Such methods will broadly empower and inform the synthesis and development of safer, more effective, and more efficient nanotechnologies that use nanoparticles with defined functions.

Keywords

Dual analyte; Single particle ICPMS; Inductively coupled plasma mass spectrometry; Nanoparticles; Quadrupole Mass Spectrometry; Alloy Nanoparticles; Kinetics

Table of Contents Graphic

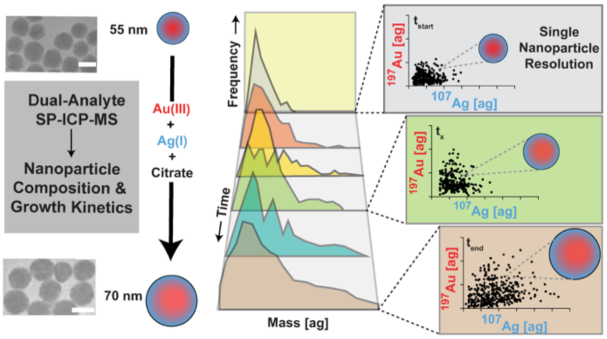

Chemical composition governs nanoparticles' optical, magnetic, catalytic, and toxicological characteristics.[1–4] To develop nanoparticles with controlled chemical composition, cost-effective characterization techniques are needed that provide high-throughput quantitative elemental analysis data with single nanoparticle resolution *in situ*. Single particle inductively coupled plasma mass spectrometry (SP-ICPMS) offers *in situ* mass quantification of individual colloidal nanoparticles.[5,6] Due to their affordability and cost-efficiency, most ICPMS instruments rely on quadrupole mass analyzers.[7] In single particle mode, quadrupoles permit the analysis of only one analyte (or isotope) per nanoparticle.[8] While quadrupole SP-ICPMS systems have obtained qualitative detection of multielement nanoparticle solutions, these approaches cannot efficiently detect two isotopes simultaneously and lack data on individual nanoparticle mass, chemical composition, and chemical kinetics.[9–11] Other ICPMS systems, like ICP-time-of-flight MS (ICP-TOF-MS) efficiently analyze 40+ isotopes of both engineered and naturally occuring nanoparticles.[12–14] However, ICP-TOF-MS instruments can be cost-prohibitive and are not as widely available as quadrupole ICPMS systems.

Other elemental analysis techniques like energy-dispersive X-ray spectroscopy (EDS) combined with scanning transmission electron microscopy (STEM) provides valuable elemental mapping of individual nanoparticles.[15] However, EDS/STEM analyses require dried samples and are limited by the number of nanoparticles within a field of view, which restricts sample size.[16] Although gaining traction, *in situ* electron microscopy analysis of nanoparticle composition remains technically challenging and may expose nanoparticle samples to free radicals, which may complicate the monitoring of chemical reactions at the single nanoparticle level.[17,18]

Here, we established *in situ* dual analyte quadrupole SP-ICPMS as a readily-accessible analytical tool for quantifying the chemical composition and reaction kinetics of individual nanoparticles *in situ*. We used a commonly-available quadrupole-based ICPMS instrument to simultaneously quantify the mass of two different isotopes in single colloidal nanoparticles. We validated the quadrupole mass analyzer's capabilities with ICP-TOF-MS and EDS/STEM. Our work demonstrates the feasibility of dual analyte quadrupole SP-ICPMS to quantify chemical transformations and reaction kinetics at the single nanoparticle level *in situ* for hundreds of bimetallic nanoparticles within seconds.

Figure S1 depicts the steps of dual analyte SP-ICPMS. Briefly, a dispersion of individual intact particles enters an inductively coupled argon plasma where the particles are atomized and ionized, resulting in a discrete ion cluster for each particle termed the transient ion cloud. Depending on particle mass, transient ion clouds last hundreds of microseconds.[19] For quadrupole ICPMS, microsecond duration times of transient ion clouds impede efficient quantification of more than one isotope (or analyte) per particle. To enable simultaneous dual isotope quantification on single nanoparticles using quadrupole ICPMS, we optimized three ICPMS parameters: 1) collision cell parameters, 2) quadrupole mass analyzer settling time, and 3) detector dwell time. The detailed optimization procedure is described in Supporting Information.

To validate quadrupole ICPMS's dual analyte capabilities at the single particle level, we used ICP-TOF-MS, *i.e.*, CyTOF (Helios, Fluidigm) and commercially available lanthanide-doped polymer beads. We compared the simultaneous detection of two isotopes per bead for three different isotope pairs: (i) ^{175}Lu and ^{140}Ce; (ii) ^{175}Lu and ^{153}Eu; and (iii) ^{175}Lu and ^{165}Ho. Using optimized dual analyte SP-ICPMS conditions, ~97% of detected beads were positive for each isotope for all three pairs of isotopes (Figure S5, Table S4). Similarly, CyTOF determined ~99% of detected beads were positive for each isotope for the same three isotope pairs (Figure S6). Notably, both techniques provided nearly equivalent results, validating our newly established and economical SP-ICPMS approach for the simultaneous detection of two different isotopes within single particles.

Upon validating quadrupole SP-ICPMS with CyTOF, we then quantified paired isotope events originating from single nanoparticles consisting of two different isotopes (Figure 1A). As model nanoparticles, we used in-house synthesized 100-nm silver nanoparticles (AgNPs) which naturally contain nearly equal amounts of ^{107}Ag and ^{109}Ag.[20] Table S5 and Figure S7 summarize the physicochemical characterization of 100-nm AgNPs. We observed that >95% of detected events were positive for both silver isotopes at nanoparticle concentrations of $1\text{x}10^5$ AgNPs/mL (Figure 1C). Figure S8 shows the real-time signal of both silver isotopes for the corresponding transient AgNP ion clouds. We observed a decrease in paired isotope events with increasing AgNP concentration. This could be due to an increase in the ion background signal at high nanoparticle concentrations (i.e. $>3\text{x}10^5$ nanoparticles/mL). As suggested by the Poisson model, the ion clouds from multiple individual nanoparticles may overlap at such concentrations resulting in an overall increased ion background.[21] The increased ion background may then impede the event pairing within the Syngistix™ software, which requires three consecutive pulse signals from each isotope to be 3σ above the background.[22] Consequently, nanoparticle concentrations of $\sim 1\text{x}10^5$ nanoparticles/mL are optimal for quantifying two isotopes from the same nanoparticle (Figure 1C).

We then quantified the number of paired events from a 1:1 mixture of 100-nm gold nanoparticles (AuNPs) and AgNPs, *i.e.*, events positive for ^{197}Au and ^{107}Ag. We hypothesized that since these isotopes originated from different nanoparticles, the detected events would remain unpaired (Figure 1B). In Table S5, Figures S7, and S9, we provide characterization of the 100-nm AuNPs. The real-time SP-ICPMS signals in Figure S10 show non-overlapping transient ion clouds for both AuNPs and AgNPs. Our dual analyte SP-ICPMS results confirmed that the nanoparticle mixture was indeed 1:1 for all nanoparticle concentrations (Figure 1D). We observed an increase in paired ^{107}Ag and ^{197}Au events with increasing nanoparticle concentrations indicating that ion signals from overlapping AgNPs and AuNPs were 3σ above the background signal and therefore automatically paired by the Syngistix^{TM} software (Figure 1E). Collectively, our data suggest that concentrations of ≤1x10^5 nanoparticles/mL are optimal for accurate dual analyte SP-ICPMS, thus enabling an analysis rate of ~300 individual nanoparticles/minute.

We then applied our dual analyte SP-ICPMS method to quantify AgNP mass. We first synthesized and characterized four differently sized AgNPs (30-, 50-, 70-, and 100-nm AgNPs) (Figure S7 and Table S5). Using SP-IPCMS, we observed increased transient nanoparticle ion cloud duration times and intensities for both silver isotopes as AgNP mass (i.e. size) increased (Figure S11). Interestingly, 30-nm AgNPs had 75% paired events for ^{107}Ag and ^{109}Ag indicating that ~25% of both silver isotopes from 30-nm AgNPs fell below the 3σ pairing criterion of the Syngistix^{TM} software (Figure S12). The observed loss in these paired events could be due to the fast microsecond detector dwell time, which may not allow sufficient time for simultaneous ion sampling per event causing both isotopes from ≤30-nm nanoparticles to become undetectable.[8] These results imply a nanoparticle mass limit of ~30 nm for dual analyte SP-ICPMS. In single analyte SP-ICPMS, however, we and others have found that ~15-nm nanoparticles can be efficiently quantified.[23,24]

For 50-, 70-, and 100-nm AgNPs, our dual analyte SP-ICPMS results in Figure 2 show that 95% of the detected events were positive for both ^{107}Ag and ^{109}Ag. To obtain nanoparticle size distributions based on the measured masses, we assumed AgNPs exhibited a spherical geometry and used Equation 1 to calculate the corresponding diameters.

$$d[nm] = \sqrt[3]{\frac{6 \cdot NPmass}{\pi \cdot \rho}} \qquad \text{Equation 1}$$

Where NPmass is the reported SP-ICPMS mass in [g] unit of a single AgNP for one isotope, and ρ is the density of silver (10.49 g/cm^3).

Using Equation 1 and the AgNP mass distributions, we obtained size distributions for the three differently sized AgNPs (Figures 2D-F). Table S6 reports the median masses and calculated sizes for all differently sized AgNPs. To confirm these results, we analyzed the same nanoparticles using transmission electron microscopy (TEM) (Figures 2G-I) and found that the nanoparticle size distributions obtained with TEM corroborated the dual analyte SP-ICPMS findings. We also determined that surface modifications such as the addition of polyethylene glycol on the surfaces of AgNPs did not affect dual analyte SP-ICPMS measurements (Figure S13). In summary, our dual analyte SP-ICPMS method accurately quantified two isotopes per nanoparticle *in situ* at a rate of over 300 particles/minute.

After simultaneously quantifying two different isotopes of the same element within single nanoparticles, we used dual analyte SP-ICPMS to quantify masses of different elements within the same nanoparticle. To accomplish this, we used in-house synthesized bimetallic gold/silver alloy nanoparticles. EDS/STEM confirmed that the alloy nanoparticles were composed of both gold and silver (Figures 3A-D) with a composition of ~60 % atomic gold and ~40% atomic silver (Table S7). TEM analysis of the alloy nanoparticles revealed the average nanoparticle diameter was 77.1±10.2 nm (Figure 3E). Conventional ensemble measurements (*i.e.,* dynamic light scattering and UV-Vis) were in line with previous reports and confirmed the successful synthesis of quasi monodisperse gold/silver alloy nanoparticles (Table S5) (Figure S7).[25,26]

We then performed dual analyte SP-ICPMS on these gold/silver alloy nanoparticles (Figure 3F). Real-time SP-ICPMS signals of the transient ion clouds (Figure S14) and the high positivity rate (>95%) for both ^{197}Au and ^{107}Ag confirmed the bimetallic nature of these alloy nanoparticles.

The mass distribution results in Figure 3F represent ~300 individual gold/silver alloy nanoparticles with absolute amounts of ^{197}Au and ^{107}Ag indicating a heterogeneous composition for individual gold/silver alloy nanoparticles.

We determined the median ^{197}Au and ^{107}Ag masses to be 3,261 ag and 1,925 ag, respectively. Based on these single nanoparticle mass distributions, we quantified the distribution of ^{197}Au and ^{107}Ag for each gold/silver alloy nanoparticle. Figure 3G shows the distribution of compositions using equations S2 and S3. At the single nanoparticle level, the average gold and silver element composition was 60% and 40%, respectively, (Figure 3G), which was previously confirmed by our quantitative EDS/STEM results.

To further explore the capabilities of our dual analyte SP-ICPMS method, we analyzed alloy nanoparticles of similar size made with two different compositions: (i) 70% Au / 30% Ag, and (ii) 30% Au / 70% Ag (Figure S15). Our dual analyte SP-ICPMS measurements revealed that these alloy nanoparticles had average compositions of 69% Au / 31% Ag and 25% Au / 75% Ag, respectively, which was also corroborated with quantitative EDS/STEM analysis (Table S7). Dual analyte SP-ICPMS provided accurate and robust mass and elemental distribution data for hundreds of individual bimetallic nanoparticles with varying compositions *in situ* within seconds.

Inspired by our dual analyte SP-ICPMS results, we sought to quantify compositional transformations in individual nanoparticles. As a model system, we exposed 80-nm gold/silver alloy nanoparticles to KI/I_2 solution, which efficiently dissolves AuNPs.[2,27,28] We started by evaluating the gold/silver alloy nanoparticle composition upon exposure to different KI/I_2 etchant concentrations with EDS/STEM (Figures 4A-D). EDS/STEM results showed a gradual decrease in gold signal (red) and a more pronounced silver signal (cyan) on the outer edges of the nanoparticles with increasing KI/I_2 etchant concentrations (Figure S16). Quantitative analysis of the EDS/STEM images revealed that the atomic percentage of gold decreased by ~3%, ~15%, and ~33%, when we exposed the gold/silver alloy nanoparticles to 68-µM, 102-µM, and 136-µM KI/I_2 etchant, respectively (Figures 4A-D, Table S7). These results demonstrated the concentration-dependent KI/I_2 etching of gold from the gold/silver alloy nanoparticles.

We then used dual analyte SP-ICPMS to obtain the mass distributions for ^{197}Au and ^{107}Ag isotopes from hundreds of individual colloidally dispersed gold/silver alloy nanoparticles exposed to different KI/I_2 etchant concentrations *in situ* (Figures 4E-H). Figures 4E-H showcase heterogenous removal of gold from individual alloy nanoparticles with increasing etchant concentration. We observed that gold was not completely removed from all of the alloy nanoparticles upon etchant exposure, which could indicate nanoparticle surface passivation.[29] At the highest etchant concentration, ^{107}Ag and ^{197}Au paired events decreased to ~68% (Figure 4H). The decrease in paired events may be due to an increased dissolved gold background at the highest etchant concentration. As both ^{107}Ag and ^{197}Au signals need to have consecutive pulses that are 3σ above the background to be automatically paired by the Syngistix™ software, an increased gold ion background could interfere with the pairing process. Notably, the increased gold ion background did not appear to affect the detection of single ^{197}Au events.

Based on the mass distributions in Figures 4E-H, we provide the average ^{107}Ag and ^{197}Au masses of five independent dual analyte SP-ICPMS measurements of alloy nanoparticles exposed to KI/I_2 etchant in Figure 4I. Since the average mass of silver per alloy nanoparticle remained relatively constant, these results suggest a predominant etching of gold. To validate these results, we performed control experiments with a 1:1 mixture of similarly sized AuNPs and AgNPs exposed to etchant solution. We observed the near-complete dissolution of AuNPs and a slight decrease in AgNPs mass upon KI/I_2 etchant exposure (Figure S17) validating that the etching reaction was predominantly toward gold.

To compare our dual analyte SP-ICPMS and EDS/STEM results, we calculated the composition of individual gold/silver alloy nanoparticles based on Figures 4E-H. The average ^{197}Au isotope mass decreases were 3%, 10%, and 26% for gold/silver alloy nanoparticles exposed to 68-µM, 102-µM, and 136-µM etchant, respectively, which we corroborated by EDS/STEM analysis (Table S7). Figure 4J summarizes the obtained ^{197}Au mass distributions for hundreds of individual gold/silver alloy nanoparticles upon exposure to different KI/I_2 etchant concentrations. As shown by our dual analyte SP-ICPMS data in Figure 4, individual gold/silver alloy nanoparticles underwent chemical etching reactions with various levels of efficiency.

We then sought to quantify the kinetics of metal deposition on individual colloidally dispersed nanoparticles with dual analyte SP-ICPMS *in situ*. As a model nanoparticle system, we selected gold/silver alloy nanoparticles and quantified the simultaneous deposition of gold and silver on these nanoparticles over time. Figure 5A, shows the process of adding Au(III) and Ag(I) ions to gold/silver alloy nanoparticles resulting in growth and thus a mass increase of individual nanoparticles over time.

We used 55-nm gold/silver alloy nanoparticles as the starting material for the seed-mediated nanoparticle growth (Figure 5A-B). TEM analysis confirmed that these gold/silver alloy nanoparticle seeds exhibited an average diameter of 56.3±5.2 nm (Figures 5B and S18). Dual analyte SP-ICPMS reported that the average masses of ^{197}Au and ^{107}Ag in individual 55-nm gold/silver alloy nanoparticles were 1,882 ag and 1,070 ag, respectively, with an initial gold and silver composition of 61% and 39%, respectively (Figures S19 and S20).

To increase the size of gold/silver alloy nanoparticles from 55 nm to 70 nm, we simultaneously added equal molar amounts of Au(III) and Ag(I) ions to a boiling aqueous dispersion containing 55-nm gold/silver alloy nanoparticles with the reducing agent sodium citrate (Figure 5A).[30] At specified time points during the chemical reaction, we analyzed the nanoparticle reaction mixture with dual analyte SP-ICPMS to simultaneously quantify the deposition of both gold and silver onto the 55-nm alloy nanoparticle seeds. Figure S20 shows the mass distribution plots for ^{197}Au and ^{107}Ag. In Figures 5C-D, we summarized our dual analyte SP-ICPMS results by showing ^{197}Au (Figure 5C) and ^{107}Ag (Figure 5D) mass distributions for individual nanoparticles over time. These data demonstrate the heterogeneity of gold and silver deposition at the single nanoparticle level over time.

Based on Figures 5C-D, we obtained the average alloy nanoparticle composition at specified time points. One minute after adding Au(III) and Ag(I) ions, the nanoparticle composition changed by 5% resulting in an average composition consisting of 66% gold and 34% silver (Figure 5E). We corroborated the relatively fast deposition of gold by UV-Vis spectrophotometry of the colloidal nanoparticle dispersion. The absorption maximum shifted from 480 nm at t_{zero} to 512 nm one minute after the addition of Au(III) and Au(I) ions to the nanoparticle seeds, indicating gold deposition (Figure S21).

At t_{2min}, the average alloy nanoparticle composition decreased to ~30% for silver, whereas the average nanoparticle composition for gold increased to ~70% (Figure 5E). Five minutes into the reaction, an average composition of 65% gold and 35% silver (Figure 5E) was observed. The element compositions obtained from the isotope mass distributions showed that after 10 minutes the average gold composition remained at ~64%, whereas the average silver composition remained at ~36% (Figure 5E). These results were corroborated by the UV-Vis spectrophotometry measurements, which stabilized at an absorption maximum of 500 nm after 15 minutes (Figure S21) suggesting the growth reaction was completed within ~15 minutes.

To obtain the reaction kinetics, we plotted the total detected mass of ^{197}Au and ^{107}Ag of the gold/silver alloy nanoparticles from Figures 5C-D as a function of time in Figure 5F. With these data, we calculated the rate constants for gold and silver depositing onto the alloy nanoparticles using Equation 2, which accounts for an exponential growth phase followed by a plateau in mass.

$$Mass_{Tn} = Mass_{T60} - (Mass_{T60} - Mass_{T0}) * e^{-k*T_n} \qquad \text{Equation 2}$$

Where $\mathrm{Mass_{Tn}}$ is the total isotope mass of all detected nanoparticles at a specific time point; $\mathrm{Mass_{T60}}$ is the total isotope mass of all detected nanoparticles at 60 minutes; $\mathrm{Mass_{T0}}$ is the total isotope mass of all detected nanoparticles before the reaction; K is the rate constant for a specific isotope; T_n is time in units of minutes.

Using Equation 2, we calculated that the deposition of gold was ~2 times faster than the deposition of silver with rate constants of 0.08 and 0.13 $\mathrm{min^{-1}}$, respectively. The observed faster deposition of gold onto the alloy nanoparticles is likely due to the differences in reduction potentials of $\mathrm{Au^{3+}/Au}$ and $\mathrm{Ag^{+}/Ag}$.[31] Our single particle analysis suggests that gold deposition was 50% complete within 5 minutes, whereas silver deposition was 50% complete within 9 minutes indicating that the reaction would be virtually complete near the 15 minute mark as previously observed with our UV-Vis spectrophotometry characterization (Figure S21). Collectively, these results showcase the feasibility for simultaneously quantifying chemical reaction kinetics of two different metals on individual nanoparticles in a high-throughput manner with easily accessible quadrupole ICPMS technology.

In summary, we established dual analyte SP-ICPMS as a quantitative high-throughput analytical technique that enables the simultaneous quantification of two analytes (or isotopes) per nanoparticle *in situ*. Our dual analyte SP-ICPMS results were obtained using a commonly available quadrupole-based ICPMS system. The results were corroborated by time-of-flight mass spectrometry and EDS/STEM. With our SP-ICPMS approach, we quantified the masses of individual AgNPs and the heterogeneity of bimetallic nanoparticles undergoing chemical reactions with high throughput (300+ nanoparticles/minute) *in situ*. Our economical elemental analysis method has the potential to transform the understanding of nanoparticle compositional evolution and transformation in environmental and biological milieus to inform the design of safer, more effective, and more efficient nanotechnologies.

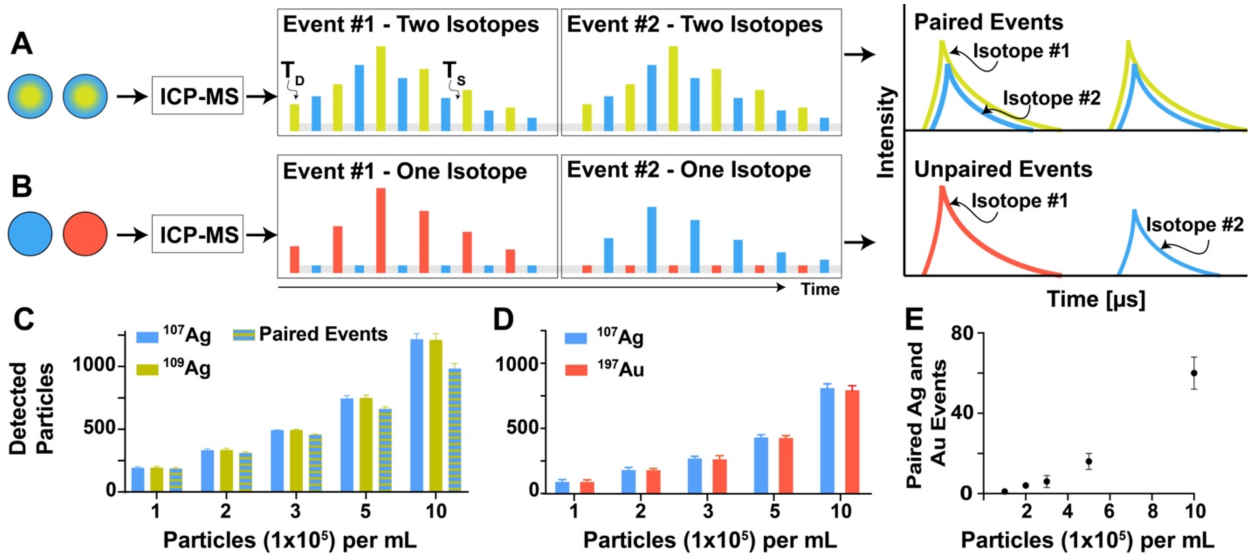

Figure 1: Quantifying paired and unpaired isotope events in dual analyte quadrupole SP-ICPMS mode for individual nanoparticles. **A.** Schematic representation of paired events for two different isotopes (blue and green) in the same nanoparticle, where T_D is the detector dwell time and T_s is the quadrupole mass filter settling time. Gaussian fits were applied by the Syngistix^{TM} software to account for the missed sample points as the quadrupole mass analyzer alternated between the two isotopes. **B.** Schematic representation of unpaired events for two different isotopes (blue and red) in different nanoparticles (blue and red). **C.** Detection of paired isotope events (^{107}Ag and ^{109}Ag) using 100-nm silver nanoparticles (AgNPs) as a function of nanoparticle concentration; mean +/- StD, n=5. **D.** Detected particles of a 1:1 mixture of 100-nm AgNPs and 100-nm gold nanoparticles (AuNPs) as a function of nanoparticle concentration; mean +/- StD, n=5. **E.** Detected paired isotope events from the 1:1 mixture of 100-nm AgNPs and AuNPs as a function of nanoparticle concentration; mean +/- StD, n=5. For all measurements, the scan time was 30 seconds.

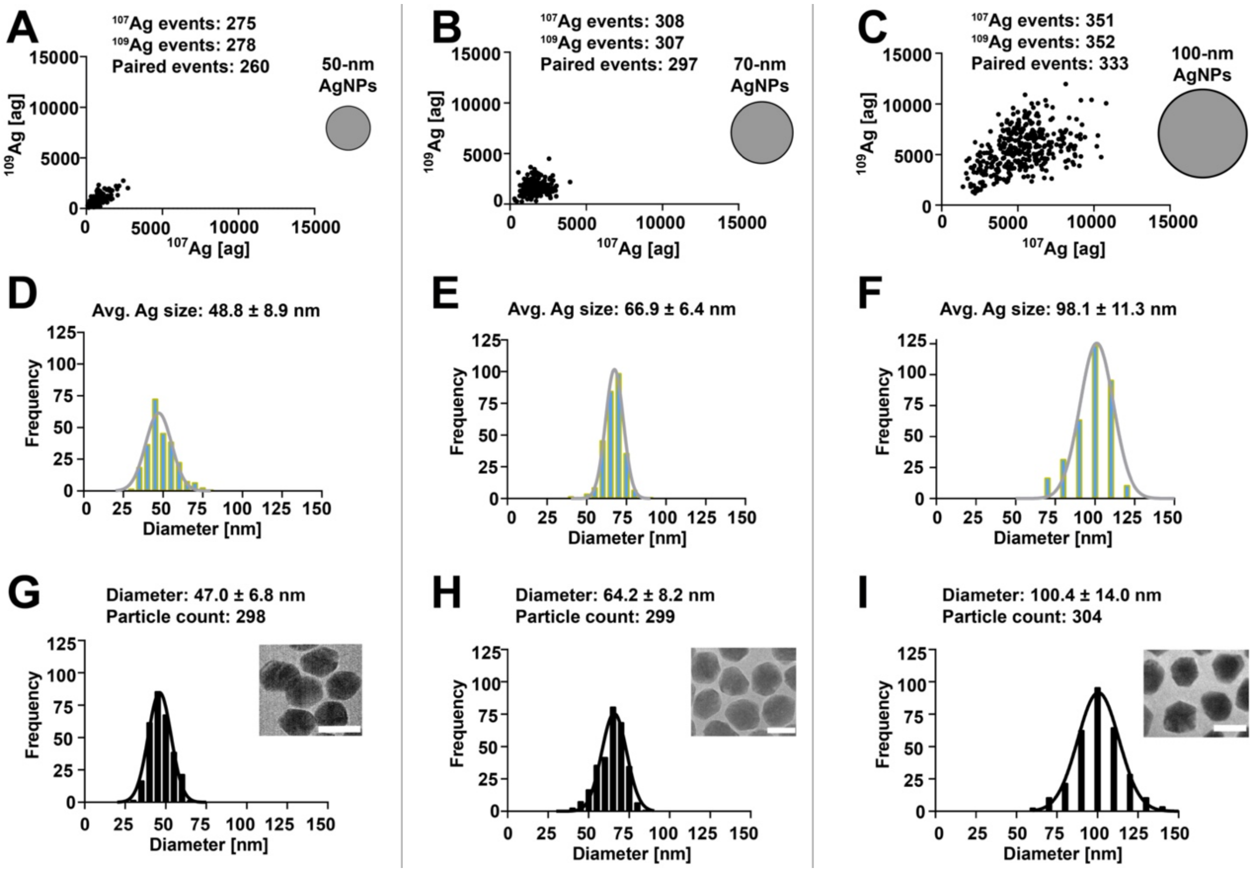

Figure 2: Single particle analysis of 50-nm, 70-nm, and 100-nm silver nanoparticles (AgNPs) using dual analyte SP-ICPMS mode. A-C. Mass distributions of differently sized AgNPs based on both silver isotopes (^{107}Ag and ^{109}Ag). **D-F.** Size distribution histograms of differently sized AgNPs for both silver isotopes based on dual analyte SP-ICPMS mass distributions values represent averages and standard deviations. **G-I.** Nanoparticle size distribution histograms based on TEM with representative micrographs values represent averages and standard deviations. Scale bars represent 50 nm, 70 nm, and 100 nm, respectively. Gaussian curves were fitted to frequency distributions in GraphPad Prism.

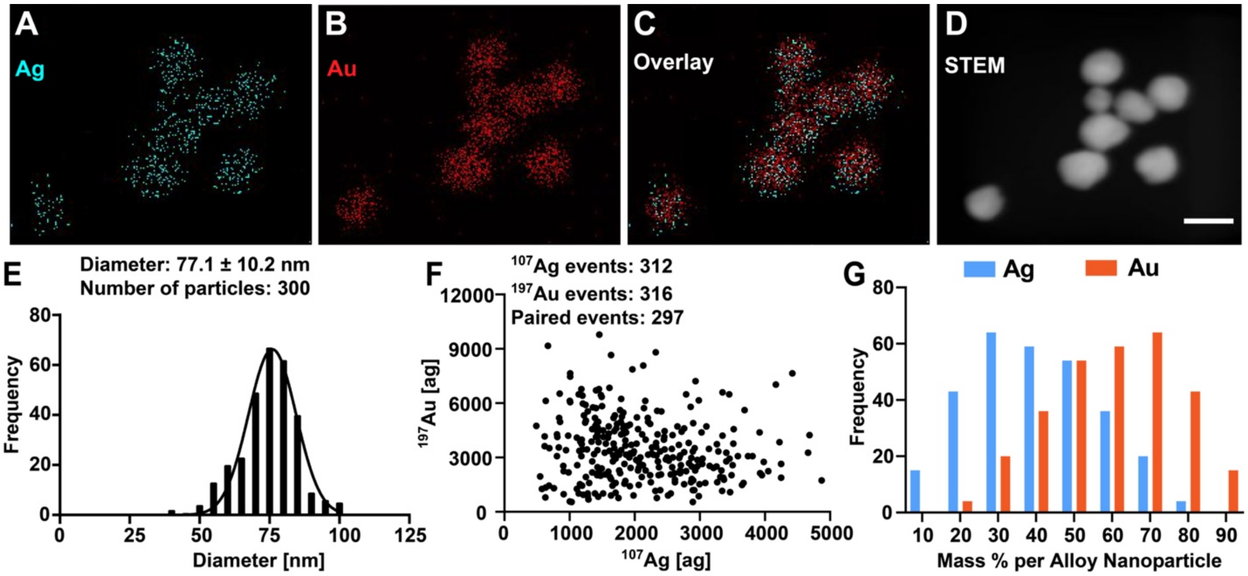

Figure 3: Compositional analysis of individual 80-nm gold/silver alloy nanoparticles (Au/AgNPs). A-D. EDS/STEM of 80-nm Au/AgNPs, where **A.** represents the EDS/STEM signal from silver in cyan; **B.** represents the EDS/STEM signal from gold in red; **C.** represents the overlay of gold and silver EDS/STEM signals. **D.** STEM image of 80-nm Au/AgNPs. Scale bar represents 100 nm. **E.** Size distribution histogram of 80-nm Au/AgNPs obtained from TEM imaging values represent averages and standard deviation. **F.** Mass distribution of individual 80-nm Au/AgNPs obtained with dual analyte SP-ICPMS mode. **G.** Mass % distribution of silver and gold isotopes for individual 80-nm Au/AgNPs obtained with dual analyte SP-ICPMS.

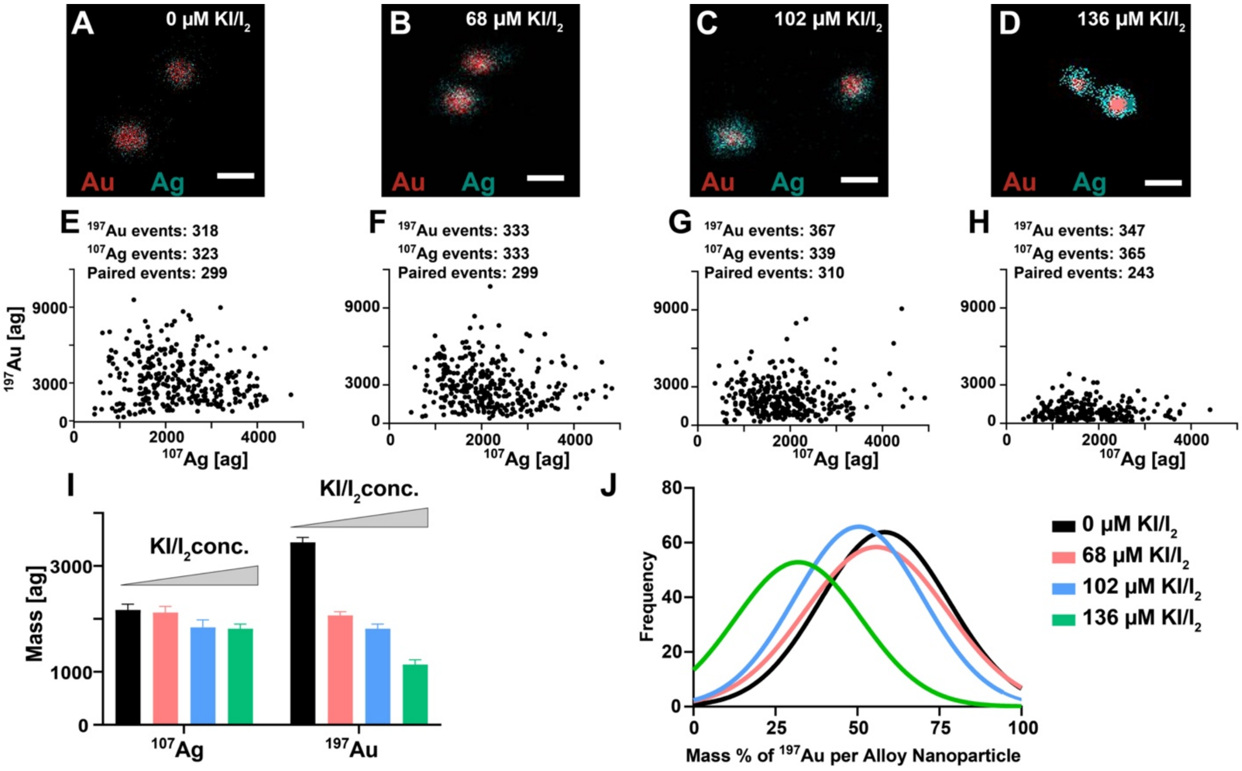

Figure 4: Quantifying gold etching using KI/I_2 in individual gold/silver alloy nanoparticles (Au/AgNPs) *in situ*. Gold/silver alloy nanoparticles with an average diameter of 80 nm were exposed to various concentrations of KI/I_2. **A-D.** STEM/EDS of Au/Ag alloy nanoparticles exposed to 0-µM, 68-µM, 102-µM, and 136-µM KI/I_2, respectively. Scale bars represent 100 nm. **E-H.** Mass distributions of individual 80-nm Au/Ag alloy nanoparticles exposed to 0-µM, 68-µM, 102-µM, and 136-µM KI/I_2, respectively, as obtained using dual analyte SP-ICPMS mode. **I.** Average masses of individual Au/Ag alloy nanoparticles particles. Bars represent the mean values and standard deviations of five measurements. **J.** Mass % distribution of ^{197}Au remaining in individual Au/Ag alloy nanoparticles based on dual analyte SP-ICPMS mass distributions from panels (E-H).

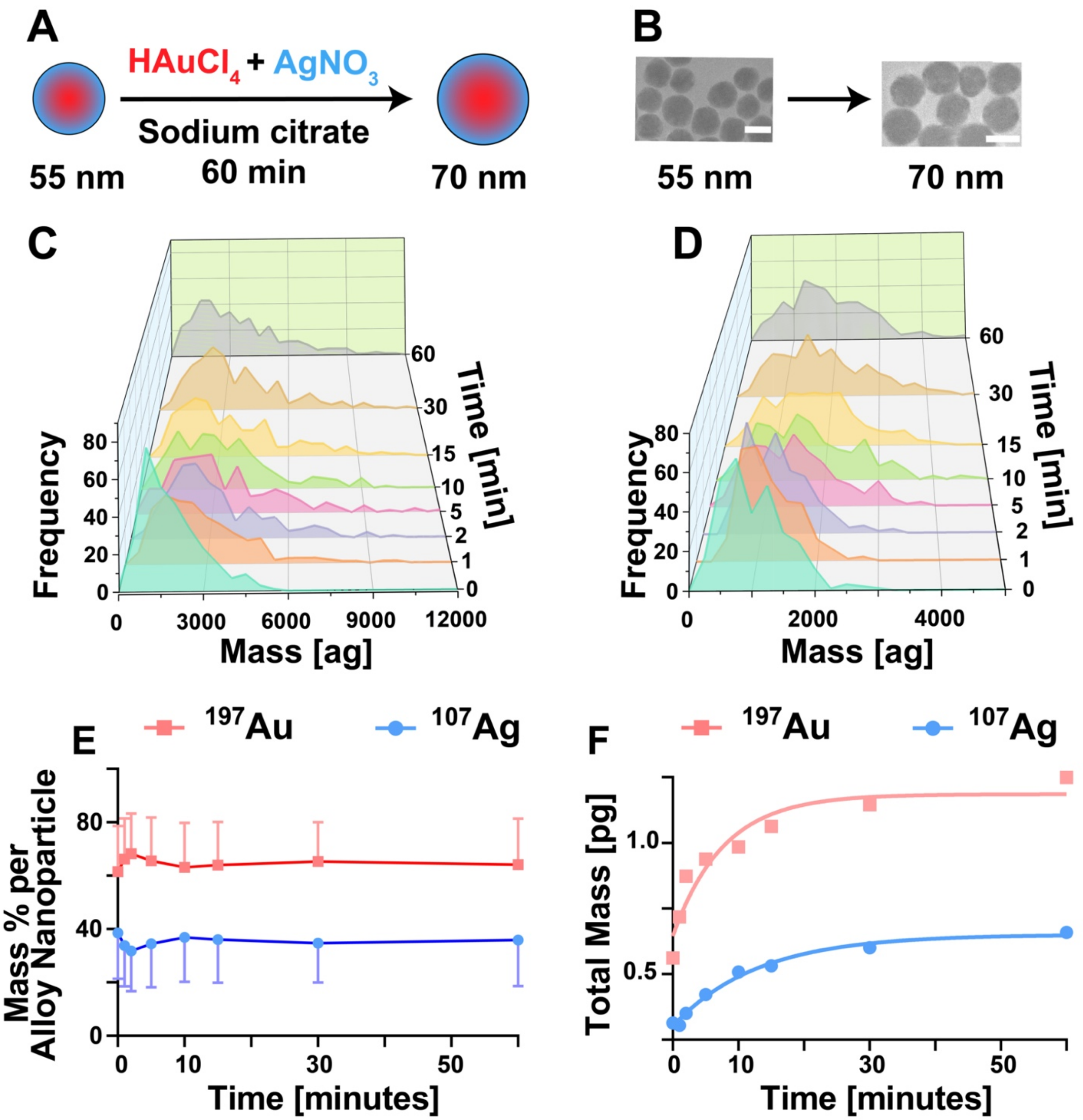

Figure 5: Quantifying metal deposition kinetics on individual gold-silver alloy nanoparticles *in situ*. A. Schematic representation of seed-mediated nanoparticle growth using 55-nm gold-silver alloy nanoparticles as seeds. **B.** TEM micrographs of (left) 55-nm gold-silver alloy nanoparticles (scale bar represents 55 nm), and (right) 70-nm gold/silver alloy nanoparticles (scale bar represents 70 nm). **C,D.** Mass distributions of ^{197}Au (**C**) and ^{107}Ag (**D**) deposition on individual alloy nanoparticles as a function of time obtained with SP-ICPMS. **E.** Elemental composition of individual gold/silver alloy nanoparticles as a function of time during seed-mediated growth calculated from mass distributions in panels C and D where values represent averages and standard deviations (n=254-360, error bars were partially removed for clarity). **F.** Data points represent the sum of detected nanoparticle masses from panels C and D. ^{197}Au (red; $r^2 = 0.92$) and ^{107}Ag (blue; $r^2 = 0.99$).

Supporting Information

Figures S1-S20, Tables S1-S7, and the methods and materials.

Acknowledgments

The authors acknowledge the assistance and fruitful discussions by Drs. S. Foster, R. Merrifield, R. Forester, J. Sabisch, and S. Liang. This work was supported in part by an NSF MRI grant (1828234), NSF CAREER award (2048130), an IBEST/OUHSC seed grant for interdisciplinary research, the OU VPRP Strategic Equipment Investment grant, the OU Faculty Investment Program, an OCAST Health Research grant (HR20-106), and the Oklahoma Tobacco Settlement Endowment Trust awarded to the University of Oklahoma - Stephenson Cancer Center. The content is solely the responsibility of the authors and does not necessarily represent the official views of the Oklahoma Tobacco Settlement Endowment Trust. This work was additionally supported by the National Institute of Arthritis and Musculoskeletal and Skin Diseases (P30AR073750) and the National Institute of General Medical Sciences (U54GM104938) through the National Institutes of Health. The Presbyterian Health Foundation and the Oklahoma Center for Adult Stem Cell Research provided funding for the CyTOF equipment.

References

(1) Wilhelm, S. Perspectives for Upconverting Nanoparticles. *ACS Nano*. American Chemical Society November 28, 2017, pp 10644–10653. https://doi.org/10.1021/acsnano.7b07120.

(2) Lazarovits, J.; Chen, Y. Y.; Song, F.; Ngo, W.; Tavares, A. J.; Zhang, Y. N.; Audet, J.; Tang, B.; Lin, Q.; Cruz Tleugabulova, M.; Wilhelm, S.; Krieger, J. R.; Mallevaey, T.; Chan, W. C. W. Synthesis of Patient-Specific Nanomaterials. *Nano Lett.* **2019**, *19* (1), 116–123. https://doi.org/10.1021/acs.nanolett.8b03434.

(3) Yang, W.; Wang, L.; Mettenbrink, E. M.; Deangelis, P. L.; Wilhelm, S. Nanoparticle Toxicology. *Annu. Rev. Pharmacol. Toxicol.* **2021**, *61*, 269–289. https://doi.org/10.1146/annurev-pharmtox-032320-110338.

(4) del Barrio, M.; Cases, R.; Cebolla, V.; Hirsch, T.; de Marcos, S.; Wilhelm, S.; Galbán, J. A Reagentless Enzymatic Fluorescent Biosensor for Glucose Based on Upconverting Glasses, as Excitation Source, and Chemically Modified Glucose Oxidase. *Talanta* **2016**, *160*, 586–591. https://doi.org/10.1016/j.talanta.2016.07.062.

(5) Merrifield, R. C.; Stephan, C.; Lead, J. Determining the Concentration Dependent Transformations of Ag Nanoparticles in Complex Media: Using SP-ICP-MS and Au@Ag Core-Shell Nanoparticles as Tracers. *Environ. Sci. Technol.* **2017**, *51* (6), 3206–3213. https://doi.org/10.1021/acs.est.6b05178.

(6) Montaño, M. D.; Olesik, J. W.; Barber, A. G.; Challis, K.; Ranville, J. F. Single Particle ICP-MS: Advances toward Routine Analysis of Nanomaterials. *Anal. Bioanal. Chem.* **2016**, *408* (19), 5053–5074. https://doi.org/10.1007/s00216-016-9676-8.

(7) Don Potter. A Commercial Perspective on the Growth and Development of the Quadrupole ICP-MS Market. *J. Anal. At. Spectrom.* **2008**, *23* (5), 690–693.

https://doi.org/10.1039/B717322A.

(8) Montaño, M. D.; Badiei, H. R.; Bazargan, S.; Ranville, J. F. Improvements in the Detection and Characterization of Engineered Nanoparticles Using SpICP-MS with Microsecond Dwell Times. *Environ. Sci. Nano* **2014**, *1* (4), 338–346. https://doi.org/10.1039/c4en00058g.

(9) Zhu, Y. L.; Lian, Y. M.; Wang, J. K.; Chen, Z. P.; Yu, R. Q. Highly Sensitive and Specific Mass Spectrometric Platform for MiRNA Detection Based on the Multiple-Metal-Nanoparticle Tagging Strategy. *Anal. Chem.* **2021**, *93* (14), 5839–5848. https://doi.org/10.1021/acs.analchem.1c00065.

(10) Zhang, X. W.; Liu, M. X.; He, M. Q.; Chen, S.; Yu, Y. L.; Wang, J. H. Integral Multielement Signals by DNA-Programmed UCNP-AuNP Nanosatellite Assemblies for Ultrasensitive ICP-MS Detection of Exosomal Proteins and Cancer Identification. *Anal. Chem.* **2021**, *93* (16), 6437–6445. https://doi.org/10.1021/acs.analchem.1c00152.

(11) Naasz, S.; Weigel, S.; Borovinskaya, O.; Serva, A.; Cascio, C.; Undas, A. K.; Simeone, F. C.; Marvin, H. J. P.; Peters, R. J. B. Multi-Element Analysis of Single Nanoparticles by ICP-MS Using Quadrupole and Time-of-Flight Technologies. *J. Anal. At. Spectrom.* **2018**, *33* (5), 835–845. https://doi.org/10.1039/c7ja00399d.

(12) Hendriks, L.; Gundlach-Graham, A.; Günther, D. Analysis of Inorganic Nanoparticles by Single-Particle Inductively Coupled Plasma Time-of-Flight Mass Spectrometry. *Chimia (Aarau).* **2018**, *72* (4), 221–226. https://doi.org/10.2533/chimia.2018.221.

(13) Mehrabi, K.; Gundlach-Graham, A.; Günther, D.; Gundlach-Graham, A. Single-Particle ICP-TOFMS with Online Microdroplet Calibration for the Simultaneous Quantification of Diverse Nanoparticles in Complex Matrices. *Environ. Sci. Nano* **2019**, *6* (11), 3349–3358.

https://doi.org/10.1039/c9en00620f.

(14) Praetorius, A.; Gundlach-Graham, A.; Goldberg, E.; Fabienke, W.; Navratilova, J.; Gondikas, A.; Kaegi, R.; Günther, D.; Hofmann, T.; Von Der Kammer, F. Single-Particle Multi-Element Fingerprinting (SpMEF) Using Inductively-Coupled Plasma Time-of-Flight Mass Spectrometry (ICP-TOFMS) to Identify Engineered Nanoparticles against the Elevated Natural Background in Soils. *Environ. Sci. Nano* **2017**, *4* (2), 307–314. https://doi.org/10.1039/c6en00455e.

(15) Jiang, Y.; Wang, L.; Meunier, M.; Mirsaidov, U. Formation Pathways of Porous Alloy Nanoparticles through Selective Chemical and Electrochemical Etching. *Small* **2021**, *2006953*, 6–11. https://doi.org/10.1002/smll.202006953.

(16) Al-Zubeidi, A.; Stein, F.; Flatebo, C.; Rehbock, C.; Hosseini Jebeli, S. A.; Landes, C. F.; Barcikowski, S.; Link, S. Single-Particle Hyperspectral Imaging Reveals Kinetics of Silver Ion Leaching from Alloy Nanoparticles. *ACS Nano* **2021**, *15* (5), 8363–8375. https://doi.org/10.1021/ACSNANO.0C10150/.

(17) Zheng, H.; Meng, Y. S.; Zhu, Y. Frontiers of in Situ Electron Microscopy. *MRS Bull.* **2015**, *40* (1), 12–18. https://doi.org/10.1557/mrs.2014.305.

(18) Sutter, E.; Jungjohann, K.; Bliznakov, S.; Courty, A.; Maisonhaute, E.; Tenney, S.; Sutter, P. In Situ Liquid-Cell Electron Microscopy of Silver-Palladium Galvanic Replacement Reactions on Silver Nanoparticles. *Nat. Commun.* **2014**, *5*. https://doi.org/10.1038/ncomms5946.

(19) Fuchs, J.; Aghaei, M.; Schachel, T. D.; Sperling, M.; Bogaerts, A.; Karst, U. Impact of the Particle Diameter on Ion Cloud Formation from Gold Nanoparticles in ICPMS. *Anal. Chem.* **2018**, *90* (17), 10271–10278. https://doi.org/10.1021/acs.analchem.8b02007.

(20) Lu, D.; Liu, Q.; Zhang, T.; Cai, Y.; Yin, Y.; Jiang, G. Stable Silver Isotope Fractionation in the Natural Transformation Process of Silver Nanoparticles. *Nat. Nanotechnol.* **2016**, *11* (8), 682–686. https://doi.org/10.1038/nnano.2016.93.

(21) Laborda, F.; Gimenez-Ingalaturre, A. C.; Bolea, E.; Castillo, J. R. About Detectability and Limits of Detection in Single Particle Inductively Coupled Plasma Mass Spectrometry. *Spectrochim. Acta Part B At. Spectrosc.* **2020**, *169*, 105883. https://doi.org/10.1016/J.SAB.2020.105883.

(22) Dan, Y.; Ma, X.; Zhang, W.; Liu, K.; Stephan, C.; Shi, H. Single Particle ICP-MS Method Development for the Determination of Plant Uptake and Accumulation of CeO2 Nanoparticles. *Anal. Bioanal. Chem.* **2016**, *408* (19), 5157–5167. https://doi.org/10.1007/s00216-016-9565-1.

(23) Newman, K.; Metcalfe, C.; Martin, J.; Hintelmann, H.; Shaw, P.; Donard, A. Improved Single Particle ICP-MS Characterization of Silver Nanoparticles at Environmentally Relevant Concentrations. *J. Anal. At. Spectrom.* **2016**, *31* (10), 2069–2077. https://doi.org/10.1039/C6JA00221H.

(24) Donahue, N. D.; Francek, E. R.; Kiyotake, E.; Thomas, E. E.; Yang, W.; Wang, L.; Detamore, M. S.; Wilhelm, S. Assessing Nanoparticle Colloidal Stability with Single-Particle Inductively Coupled Plasma Mass Spectrometry (SP-ICP-MS). *Anal. Bioanal. Chem.* **2020**, *412* (22), 5205–5216. https://doi.org/10.1007/S00216-020-02783-6.

(25) Wang, C.; Peng, S.; Chan, R.; Sun, S. Synthesis of AuAg Alloy Nanoparticles from Core/Shell-Structured Ag/Au. *Small* **2009**, *5* (5), 567–570. https://doi.org/10.1002/smll.200801169.

(26) Wang, C.; Yin, H.; Chan, R. Alloy NPs and Their Catalysis for CO Oxidation. *Chem.*

Mater. **2009**, *21* (3), 2007–2009.

(27) Cho, E. C.; Xie, J.; Wurm, P. A.; Xia, Y. Understanding the Role of Surface Charges in Cellular Adsorption versus Internalization by Selectively Removing Gold Nanoparticles on the Cell Surface with a I 2/KI Etchant. *Nano Lett.* **2009**, *9* (3), 1080–1084. https://doi.org/10.1021/nl803487r.

(28) Sun, S.; Gao, M.; Lei, G.; Zou, H.; Ma, J.; Huang, C. Visually Monitoring the Etching Process of Gold Nanoparticles by KI/I2 at Single-Nanoparticle Level Using Scattered-Light Dark-Field Microscopic Imaging. *Nano Res.* **2016**, *9* (4), 1125–1134. https://doi.org/10.1007/s12274-016-1007-z.

(29) Li, X.; Chen, Q.; McCue, I.; Snyder, J.; Crozier, P.; Erlebacher, J.; Sieradzki, K. Dealloying of Noble-Metal Alloy Nanoparticles. *Nano Lett.* **2014**, *14* (5), 2569–2577. https://doi.org/10.1021/nl500377g.

(30) Rioux, D.; Meunier, M. Seeded Growth Synthesis of Composition and Size-Controlled Gold-Silver Alloy Nanoparticles. *J. Phys. Chem. C* **2015**, *119* (23), 13160–13168. https://doi.org/10.1021/acs.jpcc.5b02728.

(31) Gilroy, K. D.; Ruditskiy, A.; Peng, H. C.; Qin, D.; Xia, Y. Bimetallic Nanocrystals: Syntheses, Properties, and Applications. *Chem. Rev.* **2016**, *116* (18), 10414–10472. https://doi.org/10.1021/acs.chemrev.6b00211.